VIDYABHARATI Vidyabharati International Interdisciplinary Research Journal
ISSN 2319-4979

Green Synthesis and Comprehensive Structural, Thermophysical, and Spectroscopic Characterization of TiO_2@Fe_3O_4 Nanocomposites for Environmental Remediation

Azra Ansari
Chemistry Department, Siddharth College of, Arts, Science and Commerce, Mumbai, India

Kulwant Singh
Materials Science Division, Bhabha Atomic Research Centre, Trombay, Mumbai, India
Corresponding author: singhkw@barc.gov.in

Nandkishor Chandan
Chemistry Department, Siddharth College of, Arts, Science and Commerce, Mumbai, India

Naina Raje
Analytical Chemistry Division, Bhabha Atomic Research Centre, Trombay, Mumbai, India

Celin Acharya
Molecular Biology Division, Bhabha Atomic Research Centre, Trombay, Mumbai, India

Abstract
TiO_2@Fe_3O_4 nanocomposites (NCs) were successfully synthesized via a simple, cost-effective, and environmentally friendly green synthesis route using Fenugreek Leaves (Trigonella foenum-graecum) as a reducing and stabilizing agent. The synthesized nanocomposites were evaluated as efficient photocatalysts for the degradation of organic dyes under UV-C irradiation. The structural, morphological, thermophysical, optical, and surface properties of the synthesized nanocomposites were comprehensively characterized using X-ray diffraction (XRD), scanning electron microscopy with energy-dispersive X-ray spectroscopy (SEM–EDX), Fourier transform infrared spectroscopy (FTIR), Raman spectroscopy, Thermogravimetric–differential thermal analysis (TGA–DTA), dynamic light scattering (DLS), Zeta potential measurements, Photoluminescence (PL) spectroscopy, and X-ray photoelectron spectroscopy (XPS). XRD confirmed the formation of crystalline anatase TiO_2 and spinel Fe_3O_4 phases with crystallite sizes of 9.4–17.3 nm. SEM–EDX revealed agglomerated nanoparticles with homogeneous elemental distribution of Ti, Fe, and O, while FTIR, Raman, and XPS verified the successful formation of the TiO_2@Fe_3O_4 heterojunction. The nanocomposites exhibited excellent thermal stability up to 1000 °C, moderate colloidal stability with a zeta potential of −17.26 mV, and suppressed electron–hole recombination, as evidenced by PL analysis, indicating efficient interfacial charge separation. Photocatalytic investigations demonstrated effective degradation of Methylene Blue, Methyl Orange, and Rhodamine B, achieving degradation efficiencies of 67.71%, 71.43%, and 81.40%, respectively, after 180 min of UV-C irradiation. The degradation kinetics followed a pseudo-first-order model, with Rhodamine B exhibiting the highest degradation rate constant. The enhanced photocatalytic activity is attributed to synergistic heterojunction-mediated charge separation, efficient generation of reactive oxygen species, and the magnetic recoverability imparted by Fe_3O_4. These findings demonstrate that TiO_2@Fe_3O_4 nanocomposites are promising, magnetically recoverable photocatalysts for sustainable wastewater treatment and environmental remediation.

Keywords: *Green synthesis; TiO_2@Fe_3O_4 nanocomposites; Photocatalytic degradation; Environmental remediation; Wastewater treatment; Spectroscopic characterization; Thermophysical properties.*

1. Introduction

Water pollution caused by industrial effluents containing textile dyes, pharmaceuticals, pesticides, and other organic contaminants is a major global environmental challenge. Synthetic dyes are particularly problematic because of their complex aromatic structures, high chemical stability, toxicity, and resistance to biodegradation. Large quantities of dye-containing wastewater discharged from textile, leather, paper, printing, and dye-manufacturing industries contaminate aquatic ecosystems by reducing light penetration, inhibiting photosynthesis, and posing serious risks to human health. Consequently, the development of efficient and sustainable technologies for wastewater treatment has become an important research priority (Acosta et al., 2026; Oladipo and Mustafa, 2023).

Among advanced wastewater treatment technologies, heterogeneous photocatalysis has attracted considerable attention because it can mineralize organic pollutants into environmentally benign products under light irradiation. Semiconductor photocatalysts generate electron–hole pairs that produce highly reactive oxygen species (ROS), such as hydroxyl (•OH) and superoxide ($\bullet O_2^-$) radicals, which effectively degrade organic contaminants. Titanium dioxide (TiO_2) is one of the most widely investigated photocatalysts due to its excellent chemical stability, low toxicity,

strong oxidative ability, and low cost. However, its practical application is limited by its wide band gap (~3.2 eV), rapid electron–hole recombination, and the difficulty of recovering fine TiO_2 particles from treated wastewater (Chen and Mao, 2007; Henderson, 2011; Hashimoto et al. 2005).

Coupling TiO_2 with magnetic Fe_3O_4 nanoparticles to form TiO_2@Fe_3O_4 heterostructures offers an effective strategy to overcome these limitations. Fe_3O_4 provides excellent magnetic recoverability while promoting charge separation through synergistic interactions with TiO_2, thereby enhancing photocatalytic efficiency and catalyst reusability (Laurent et al. 2008; Deng and Zhao. 2015).

Green synthesis using plant extracts has emerged as a sustainable alternative to conventional chemical methods. Phytochemicals present in Trigonella foenum-graecum (fenugreek) leaves, including flavonoids, phenolics, alkaloids, and saponins, serve as natural reducing and stabilizing agents, enabling the environmentally friendly synthesis of nanomaterials without hazardous chemicals. Plant-mediated synthesis has been reported to produce TiO_2–Fe_3O_4 nanocomposites with promising physicochemical and photocatalytic properties (Iravani, 2011; Ahmed et al., 2016; Gebrezgiabher et al., 2019; Nengsiha et al., 2024; Almutairi, 2024).

Despite these advances, comprehensive studies correlating the structural, surface, optical, thermal, and colloidal properties of green-synthesized TiO_2@Fe_3O_4 nanocomposites with their photocatalytic performance remain limited, particularly for the degradation of chemically diverse dye pollutants.

Therefore, this study reports the green synthesis of TiO_2@Fe_3O_4 nanocomposites using fenugreek leaf extract, followed by comprehensive physicochemical characterization using complementary structural, morphological, optical, thermal, surface, and colloidal techniques. Their photocatalytic performance was evaluated through the degradation of methylene blue (MB), rhodamine B (RhB), and methyl orange (MO) under UV-C irradiation. By integrating green synthesis, comprehensive characterization, and multi-dye photocatalytic evaluation, this work provides valuable insights into the development of efficient, magnetically recoverable, and environmentally sustainable photocatalysts for wastewater treatment.

2. Experimental

2.1 Materials and Methods

2.1.1 Materials Used

Fresh fenugreek (Trigonella foenum-graecum) leaves were procured from a local market and used to prepare an aqueous leaf extract as a natural reducing, capping, and stabilizing agent. Titanium tetra-isopropoxide (TTIP, 27.8–28.6% TiO_2, SRL, India) served as the titanium precursor. Ferric chloride hexahydrate ($FeCl_3 \cdot 6H_2O$, ≥98%, Merck, India) and ferrous sulfate heptahydrate ($FeSO_4 \cdot 7H_2O$, ≥99%, Merck, India) were used as iron precursors for Fe_3O_4 synthesis. Ammonium hydroxide (NH_4OH, 25% w/v, Merck, India) was used as the precipitating agent, while sodium hydroxide (NaOH, ≥98%, AR grade, Merck, India) was used for pH adjustment. Ethanol (≥99.9%, AR grade, Merck, India) and deionized (DI) water were used throughout the synthesis and purification processes. All chemicals were of analytical reagent (AR) grade and used without further purification.

2.1.2 Preparation of Fenugreek Leaves Extract

Fresh fenugreek (Trigonella foenum-graecum) leaves were washed thoroughly with tap water followed by deionized water, shade-dried at room temperature, and ground into a fine powder. An aqueous leaf extract was prepared by heating 10 g of the powder with 500 mL of deionized water at 80 °C for 1 h under continuous magnetic stirring. After cooling to room temperature, the extract was filtered through Whatman No. 1 filter paper and stored at 4 °C for subsequent synthesis of TiO_2@Fe_3O_4 nanocomposites.

2.1.3 Green Synthesis of TiO_2 Nanoparticles

TiO_2 nanoparticles were synthesized via a plant-mediated green route using aqueous fenugreek (Trigonella foenum-graecum) leaf extract as a natural reducing and stabilizing agent. Briefly, 20 mL of titanium tetra-isopropoxide (TTIP) was added dropwise to 100 mL of the leaf extract under continuous magnetic stirring at room temperature. The reaction mixture was stirred for 3h until a light brown creamy precipitate formed. The precipitate was filtered, washed

repeatedly with deionized water to remove residual impurities, dried at 100 °C for 5 h, and finally calcined at 500 °C for 4 h to obtain crystalline TiO_2 nanoparticles.

2.1.4 Synthesis of TiO_2@Fe_3O_4 Nanocomposites

Fe_3O_4 nanoparticles were first synthesized via a plant-mediated green route. Briefly, 3.027 g of $FeCl_3 \cdot 5H_2O$ and 1.540 g of $FeSO_4 \cdot 7H_2O$ were dissolved in deionized water and stirred at 60 °C for 15 min. Fenugreek (Trigonella foenum-graecum) leaf extract was then added, and the mixture was stirred for a further 30 min. A 10% aqueous ammonia solution was added dropwise until a black precipitate formed, and the reaction was continued at 60 °C for 90 min. The Fe_3O_4 nanoparticles were collected by filtration, washed repeatedly with deionized water, and heated at 200 °C for 2 h.

For the synthesis of TiO_2@Fe_3O_4 nanocomposites, the dried Fe_3O_4 nanoparticles were dispersed in 10 mL ethanol by ultrasonication. Separately, 20 mL of titanium tetra-isopropoxide (TTIP) was added dropwise to 80 mL of fenugreek leaf extract under continuous stirring. The Fe_3O_4 dispersion was then added to the TiO_2 precursor solution and stirred for 30 min to form the TiO_2@Fe_3O_4 nanocomposites. The product was washed repeatedly with a 1:1 (v/v) mixture of deionized water and ethanol until neutral pH, followed by drying at 100 °C for 2 h to obtain the final nanocomposites (Fauzi et al. 2024). A schematic illustration of the green synthesis of Fe_3O_4 nanoparticles and the subsequent formation of TiO_2@Fe_3O_4 nanocomposites is shown in Fig.1.

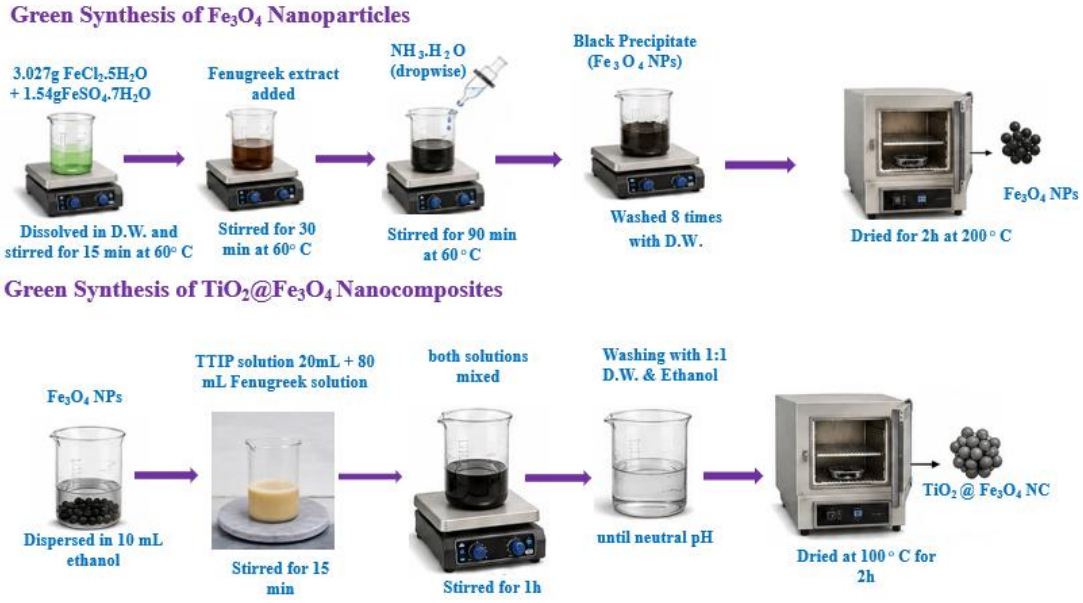


Fig.1: Schematic illustration of the stepwise synthesis of Fe_3O_4 nanoparticles and TiO_2@Fe_3O_4 nanocomposites.

2.1.5 Statistical Analysis

All experiments were performed in triplicate (n = 3), and the results are expressed as mean ± standard deviation (SD). The mean and SD were calculated from three independent experiments to ensure the accuracy and reproducibility of the results. Error bars representing SD are included in the relevant figures where applicable. The relatively small SD values indicate good experimental precision. Statistical analyses and graph plotting were performed using OriginPro 2024. The apparent pseudo-first-order rate constants (k) were determined by linear regression of the $\ln(C_0/C_t)$ versus irradiation time plots, and the goodness of fit was evaluated using the coefficient of determination (R^2).

2.2 Characterization

2.2.1 Scanning Electron Microscopy (SEM) and Energy-Dispersive X-ray Spectroscopy (EDX)

The surface morphology of the synthesized TiO_2@Fe_3O_4 nanocomposites was examined using a scanning electron microscope (SEM; Carl Zeiss EVO 18, Germany) operated at an accelerating voltage of 5.2 kV. Secondary electron (SE) images were acquired to investigate the particle

morphology and surface microstructure. Prior to analysis, the powdered samples were sputter-coated with a thin layer of gold to improve electrical conductivity and minimize charging effects.

The elemental composition of the nanocomposites was determined using an energy-dispersive X-ray spectroscopy (EDX) detector (INCA Energy 200, Oxford Instruments) integrated with the SEM. EDX analysis was performed to confirm the elemental composition of the synthesized TiO_2@Fe_3O_4 nanocomposites.

2.2.2 X-ray Diffraction (XRD)

X-ray diffraction (XRD) analysis was performed to determine the crystal structure, phase composition, phase purity, crystallinity, and crystallite size of the synthesized TiO_2@Fe_3O_4 nanocomposites. Diffraction patterns were recorded using a Rigaku MiniFlex X-ray diffractometer (Rigaku Corporation, Japan) with Cu Kα radiation (λ = 1.5406 Å) over a 2θ range of 5°–80°. The diffraction peaks were indexed by comparison with the International Centre for Diffraction Data (ICDD-PDF) database to identify the crystalline phases and confirm the coexistence of TiO_2 and Fe_3O_4 in the synthesized nanocomposites.

2.2.3 Thermogravimetric Analysis (TGA) and Differential Thermal Analysis (DTA)

Thermogravimetric analysis (TGA) and differential thermal analysis (DTA) of the synthesized TiO_2@Fe_3O_4 nanocomposites were performed using a NETZSCH STA 409 PC/PG simultaneous thermal analyzer (NETZSCH, Germany) to evaluate their thermal stability and phase transformation behavior. Approximately 50 mg of the sample was placed in an alumina (Al_2O_3) crucible, with an empty alumina crucible serving as the reference. Measurements were carried out under a nitrogen atmosphere (120 mL min^{-1}) from room temperature to 800 °C at a heating rate of 10 °C min^{-1}. The TGA curves were used to monitor mass loss associated with moisture removal, residual organic constituents, and thermal decomposition, while the DTA curves were used to identify endothermic and exothermic events related to phase transitions and crystallization.

2.2.4 Fourier Transform Infrared Spectroscopy (FTIR)

Fourier transform infrared (FTIR) spectroscopy was performed to identify the functional groups, chemical bonds, and interactions between the TiO_2 and Fe_3O_4 phases in the synthesized TiO_2@Fe_3O_4 nanocomposites. Spectra were recorded using a Bruker Tensor 27 FTIR spectrometer (Bruker Optics, Germany) equipped with a PIKE MIRacle attenuated total reflection (ATR) accessory fitted with a single-reflection diamond crystal. The spectra were collected over the range of 4000–400 cm^{-1} at a resolution of 4 cm^{-1} under ambient conditions. A background spectrum was recorded prior to each measurement, and the powdered samples were analyzed directly in ATR mode by applying gentle pressure to ensure good contact with the diamond crystal.

2.2.5 Photoluminescence (PL) Spectroscopy

Photoluminescence (PL) spectroscopy was performed to investigate the charge-carrier recombination behavior of the synthesized TiO_2@Fe_3O_4 nanocomposites. PL spectra were recorded at an excitation wavelength of 375 nm using an FLS920 fluorescence spectrometer (Edinburgh Instruments, UK) equipped with a 450 W continuous xenon arc lamp. Time-resolved photoluminescence (TRPL) decay measurements were performed using a μF900 flash lamp coupled to the same spectrometer to evaluate the charge-carrier lifetime and recombination dynamics.

2.2.6 Raman Spectroscopy

Raman spectroscopy was performed to investigate the vibrational characteristics, crystal structure, and phase composition of the synthesized TiO_2@Fe_3O_4 nanocomposites. Raman spectra were recorded using a Hawk Raman 785D portable Raman spectrometer (NAI & M, India) equipped with a 785 nm excitation laser over the Raman shift range of 100–3200 cm^{-1} at a spectral resolution of 1.0 cm^{-1} under ambient conditions. The spectra were analyzed to identify the characteristic vibrational modes of anatase TiO_2 and spinel Fe_3O_4, confirming the coexistence of both phases in the synthesized nanocomposites.

2.2.7 X-ray Photoelectron Spectroscopy (XPS)

X-ray photoelectron spectroscopy (XPS) was performed to determine the surface elemental composition and oxidation states of the synthesized TiO_2@Fe_3O_4 nanocomposites. Measurements were carried out using a SPECS XPS system equipped with a PHOIBOS 150 Delay Line Detector (DLD) analyzer and a monochromatic Al Kα X-ray source (hν = 1486.6 eV). Spectra were recorded at a pass energy of 40 eV, and the binding energy scale was calibrated using the adventitious C 1s peak at 284.8 eV. The spectra were analyzed to determine the chemical states of Ti, Fe, and O in the synthesized nanocomposites.

2.2.8 Zeta Potential

The zeta potential of the synthesized TiO_2@Fe_3O_4 nanocomposites was measured using a Litesizer 500 (Anton Paar, Austria) to evaluate their surface charge and colloidal stability. Prior to analysis, the dried nanocomposite powder was dispersed in deionized water (0.5 mg mL^{-1}) and ultrasonicated to obtain a homogeneous suspension. The dispersion was transferred to an Omega cuvette (Anton Paar), and zeta potential measurements were performed according to the manufacturer's instructions. The measured zeta potential values were used to assess the colloidal stability of the nanocomposite suspension.

2.2.9 Dynamic Light Scattering (DLS) Analysis

Dynamic light scattering (DLS) measurements were performed to determine the hydrodynamic particle size distribution and polydispersity index (PDI) of the synthesized TiO_2@Fe_3O_4 nanocomposites using a Malvern 4800 Autosizer equipped with a 7132 digital correlator. Measurements were carried out at 25 °C using a circulating water bath to maintain thermal stability. A He–Ne laser (λ = 632.8 nm, 15 mW) served as the light source, and scattered light was recorded at a scattering angle of 90°. Samples were dispersed in deionized water and analyzed in 10 mm cylindrical quartz cuvettes. Each sample was measured five times, and the reported values represent the average of these measurements. The intensity autocorrelation functions were analyzed using the cumulants method to determine the average hydrodynamic diameter and PDI.

2.2.10 UV–Visible Spectroscopy

UV–Visible (UV–Vis) spectroscopy was employed to monitor the photocatalytic degradation of organic dyes by measuring changes in their characteristic absorbance during irradiation. Absorbance measurements were performed using an Infinite® M200 PRO multimode microplate reader (Tecan, Austria). Spectra were recorded over the wavelength range of 300–750 nm using a 96-well flat-bottom polystyrene microplate, with 200 µL of each sample loaded into individual wells. Pathlength correction was applied to ensure accurate absorbance measurements. All measurements were carried out at 25 ± 1 °C using appropriate blank solutions as references.

2.3 Photocatalytic Dye Degradation Experiment

Methylene Blue (MB), Methyl Orange (MO), and Rhodamine B (RhB) were used as model organic dyes to evaluate the photocatalytic activity of the synthesized TiO_2@Fe_3O_4 nanocomposites (NCs) under UV-C irradiation.

2.3.1 Preparation of Dye Solutions

Stock solutions of Methylene Blue (MB), Methyl Orange (MO), and Rhodamine B (RhB) were prepared by dissolving 5 mg of each dye separately in 1 L of deionized (DI) water, yielding solutions with natural pH values of 8.90, 8.40, and 8.85, respectively. For each photocatalytic experiment, 100 mL of the appropriate dye solution was transferred to a 250 mL beaker. The maximum absorption wavelength (λ_{max}) of each dye was determined by recording its UV–Visible absorption spectrum prior to the photocatalytic experiments.

2.3.2 Photocatalyst Loading

For the photocatalytic degradation experiments, 0.05 g of TiO_2@Fe_3O_4 nanocomposite was dispersed in 100 mL of each dye solution. The suspension was magnetically stirred in the dark for 1 h to establish adsorption–desorption equilibrium between the dye molecules and the photocatalyst surface prior to UV-C irradiation.

2.3.3 Absorbance Measurement

The photocatalytic degradation of the dyes was monitored by UV–Visible spectroscopy. After establishing adsorption–desorption equilibrium in the dark, approximately 1.5 mL of the suspension was withdrawn and centrifuged at 3000 rpm for 3 min to separate the photocatalyst. The clear supernatant was transferred to a cuvette, and the absorbance after dark adsorption (A_0) was recorded. During UV-C irradiation, aliquots were collected at 20 min intervals up to 180 min, centrifuged under the same conditions, and the absorbance at time t (A_t) was measured.

3. Results & Discussion

3.1 SEM and EDX Analysis

The surface morphology of the synthesized $TiO_2@Fe_3O_4$ nanocomposites was examined by scanning electron microscopy (SEM), and the corresponding micrographs are presented in Fig.2(a–d). The SEM images reveal aggregated nanoparticles with irregular morphology and a rough, porous surface. Such agglomeration is commonly observed in Fe_3O_4-based magnetic nanocomposites because of strong magnetic dipole–dipole interactions and the high surface energy of nanoparticles (Kubiak, 2023).

The micrographs show interconnected nanoclusters composed of quasi-spherical to irregular particles, forming a heterogeneous porous architecture that provides a high surface area and abundant active sites for adsorption and photocatalytic reactions (Mehdinia et al., 2017). Fig.2(a) exhibits compact agglomerated domains with non-uniform particle distribution, while Fig.2(b) shows interconnected porous regions and clustered nanoparticles. Fig.2(c) reveals a sponge-like porous network with increased surface roughness, whereas Fig.2(d) displays comparatively compact and well-dispersed nanograins, indicating improved structural integrity of the nanocomposite.

Overall, the porous and rough morphology is expected to enhance dye adsorption and photocatalytic performance by increasing the number of accessible active sites. Although particle agglomeration may reduce the effective surface area, such behavior is typical of magnetic $TiO_2@Fe_3O_4$ nanocomposites (Vinosel et.al., 2017).

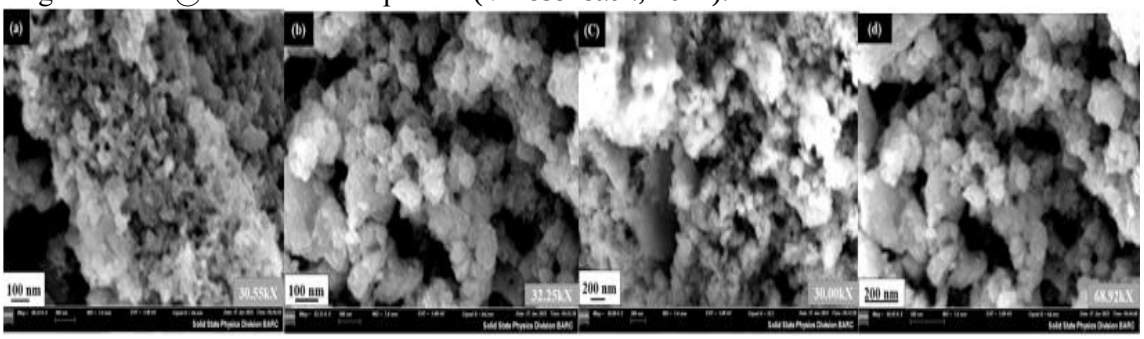


Fig.2: SEM Micrographs of the Synthesized $TiO_2@Fe_3O_4$ Nanocomposite

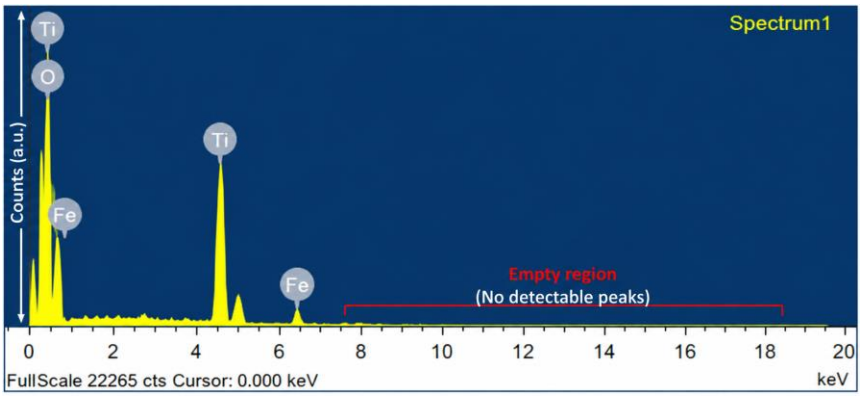
3.1.1 Elemental Composition Analysis of $TiO_2@Fe_3O_4$ Nanocomposite by EDX

The elemental composition of the synthesized $TiO_2@Fe_3O_4$ nanocomposite was analyzed by Energy Dispersive X-ray Spectroscopy (EDX), and the corresponding spectrum is shown in Fig.3. The spectrum confirms the presence of titanium (Ti), iron (Fe), and oxygen (O), consistent with the expected composition of the $TiO_2@Fe_3O_4$ nanocomposite (Goldstein et al., 2018).

The characteristic O Kα peak appears at approximately 0.52 keV, while Ti is identified by its Ti Lα (≈0.45 keV), Ti Kα (≈4.51 keV), and Ti Kβ (≈4.93 keV) peaks. Iron is confirmed by the Fe Lα (≈0.70 keV), Fe Kα (≈6.40 keV), and Fe Kβ (≈7.06 keV) peaks, verifying the coexistence of the TiO_2 and Fe_3O_4 phases.

No significant peaks corresponding to extraneous elements were detected, indicating high elemental purity within the detection limits of the technique (Denga et al., 2025). A few weak peaks in the 1–4 keV region were observed but could not be reliably assigned and are likely due to instrumental background, detector artifacts, sample-holder contributions, or trace-level impurities. These peaks were therefore excluded from the elemental interpretation.

Overall, the EDX analysis confirms the successful formation of a high-purity $TiO_2@Fe_3O_4$ nanocomposite suitable for subsequent photocatalytic investigations (Ramadhan et al., 2017).



Element	Line	Energy (keV)	Weight %	Atomic %
O	Kα	0.525	35.52	63.89
Ti	Kα	4.508	50.11	31.76
Fe	Kα	6.398	14.37	4.35

Ti – Titanium
O – Oxygen
Fe – Iron

Fig.3: EDX spectrum of the synthesized TiO_2@Fe_3O_4 nanocomposite showing its elemental composition.

3.2 XRD Analysis

The XRD pattern of the synthesized TiO_2@Fe_3O_4 nanocomposite is shown in Fig.4. Diffraction peaks at $2\theta \approx 30.1°$, 35.5°, 43.1°, 53.4°, 57.0°, and 62.6° are indexed to the (220), (311), (400), (422), (511), and (440) planes of cubic spinel Fe_3O_4 (JCPDS No. 19-0629), confirming the crystalline magnetite phase (Sembiring et al., 2025). Additional peaks at 25.3°, 37.8°, 48.0°, and 55.1° correspond to the (101), (004), (200), and (211) planes of anatase TiO_2 (JCPDS No. 21-1272), verifying the coexistence of both crystalline phases.

No impurity peaks were detected, indicating the high phase purity of the synthesized nanocomposite. The sharp diffraction peaks further demonstrate good crystallinity. The crystallite sizes, calculated using the Debye–Scherrer equation, ranged from 9.4 to 17.3 nm. These XRD results, together with the FTIR, Raman, SEM–EDX, and XPS analyses, confirm the successful synthesis of highly crystalline TiO_2@Fe_3O_4 nanocomposites suitable for photocatalytic applications.

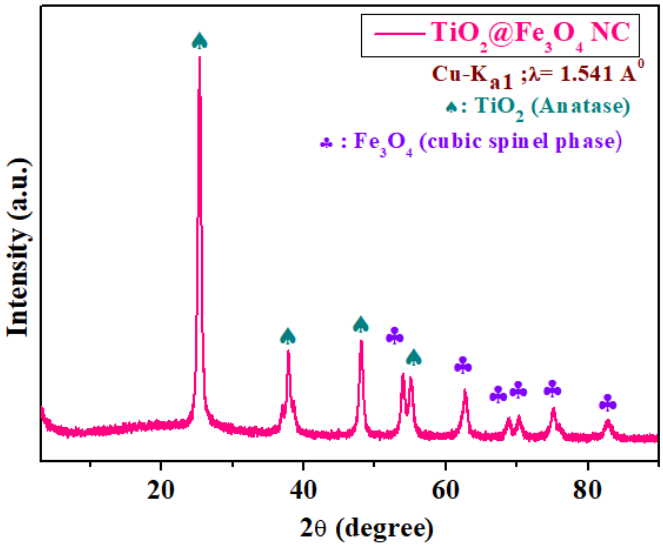


Fig.4: X-ray diffraction pattern of the synthesized TiO_2@Fe_3O_4 nanocomposite showing the characteristic diffraction peaks of crystalline Fe_3O_4 and anatase TiO_2 phases.

3.3 TGA/DTA Analysis

The thermal stability of the synthesized TiO_2@Fe_3O_4 nanocomposite was investigated by TGA/DTA from room temperature to 1000 °C, as shown in Fig.5. The TGA curve exhibits a gradual weight loss with increasing temperature, while the DTA curve reveals the corresponding thermal events.

An initial weight loss below 200–250 °C is attributed to the removal of physically adsorbed moisture and volatile surface species (Kubiak et al., 2020). Between 250 and 700 °C, gradual

mass loss results from the decomposition of residual organic species and surface-bound functional groups originating from the green synthesis process. Above 700 °C, only a slight additional weight loss is observed, indicating the high thermal stability of the oxide framework. The total weight loss is approximately 15 wt.%, with nearly 85 wt.% of the material retained after heating to 1000 °C. The DTA curve shows only broad, weak thermal events without sharp transitions, indicating the absence of significant decomposition or phase transformations.

Overall, the TGA/DTA results confirm the excellent thermal stability of the TiO_2@Fe_3O_4 nanocomposite, making it suitable for photocatalytic and environmental remediation applications requiring thermal durability (Khashan et al., 2017).

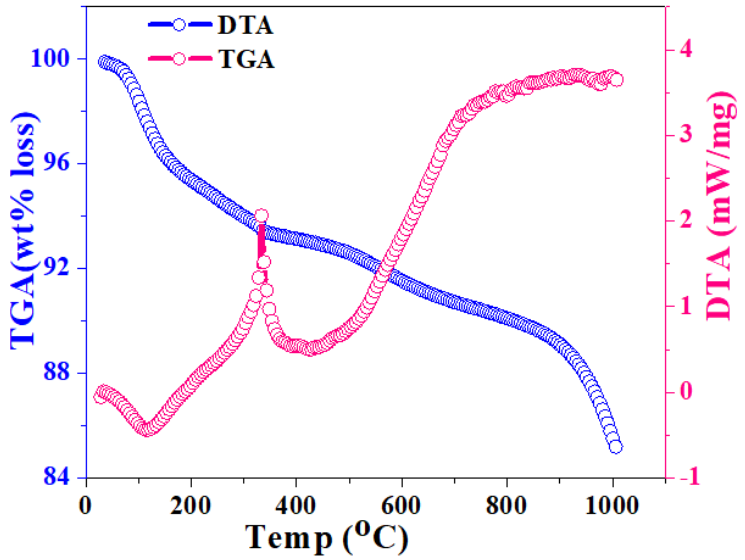


Fig.5: Simultaneous TGA and DTA analysis of the synthesized TiO_2@Fe_3O_4 nanocomposite from room temperature to 1000 °C.

3.4 Fourier Transform Infrared (FTIR) Spectroscopy Analysis

The FTIR spectrum of the synthesized TiO_2@Fe_3O_4 nanocomposite (Fig.6) was analyzed to identify the chemical bonds and surface functional groups. The observed absorption bands confirm the successful formation of the nanocomposite and the presence of residual biomolecules from the green synthesis process.

A broad band around 3400 cm^{-1} corresponds to the O–H stretching vibration of surface hydroxyl groups and adsorbed water, which serve as active sites for hydroxyl radical (•OH) generation during photocatalysis (Wojciechowska et al., 2022). The bands at 2920 and 2850 cm^{-1} are assigned to asymmetric and symmetric C–H stretching vibrations of residual plant-derived organic compounds. A weak band near 2350 cm^{-1} is attributed to atmospheric CO_2, while the band at ~1630 cm^{-1} corresponds to the bending vibration of adsorbed water molecules. The bands at 1450 and 1380 cm^{-1} are associated with oxygen-containing organic functional groups originating from the fenugreek extract, indicating their role in nanoparticle formation and stabilization (Moosavi et al. 2020). In the fingerprint region, the absorption bands at ~1100 cm^{-1}, ~650 cm^{-1}, and ~560 cm^{-1} are assigned to Ti–O–Ti, Fe–O, and Ti–O stretching vibrations, respectively, confirming the coexistence of TiO_2 and Fe_3O_4 phases in the nanocomposite.

Overall, the FTIR results confirm the formation of the TiO_2@Fe_3O_4 nanocomposite and the presence of surface hydroxyl groups and residual biomolecules. These findings, together with the XRD, SEM–EDX, Raman, and XPS results, verify the successful synthesis of the nanocomposite. The abundant surface hydroxyl groups are expected to enhance pollutant adsorption and reactive oxygen species generation, thereby improving photocatalytic performance (Pucar et al., 2022).

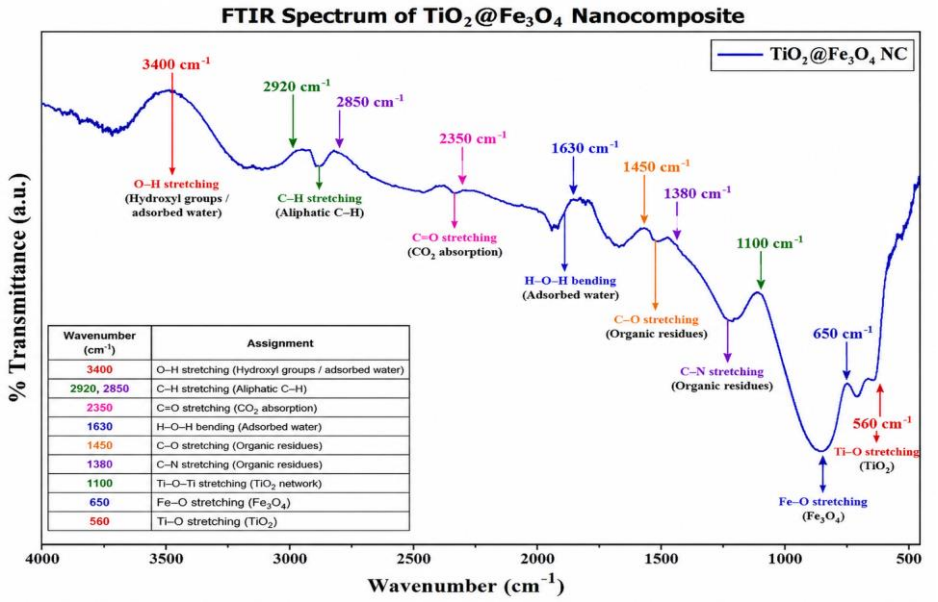


Fig.6: Fourier Transform Infrared (FTIR) spectrum of the synthesized TiO_2@Fe_3O_4 nanocomposite recorded over the wavenumber range of 4000–500 cm^{-1}.

3.5 Photoluminescence (PL) Analysis

The photoluminescence (PL) spectrum of the synthesized TiO_2@Fe_3O_4 nanocomposite is shown in Fig.7. A broad emission band extending from 450 to 800 nm, with a maximum at ~590 nm, was observed, indicating the presence of defect-related radiative recombination pathways (Banisharif, 2013).

The visible emission is mainly attributed to intrinsic defect states, including oxygen vacancies, Ti^{3+} centers, surface hydroxyl groups, and interfacial defects, which introduce localized energy levels within the band gap. These defect sites act as charge-carrier trapping centers, suppressing rapid electron–hole recombination and prolonging charge-carriers lifetime, thereby promoting the generation of reactive oxygen species for photocatalytic reactions.

The absence of distinct band-edge emission indicates that defect-mediated luminescence dominates the PL response. The broad visible emission is consistent with the defect-rich structure revealed by XPS and other characterization techniques, confirming favorable electronic properties for enhanced photocatalytic and environmental remediation applications (Aguinaco et al. 2022).

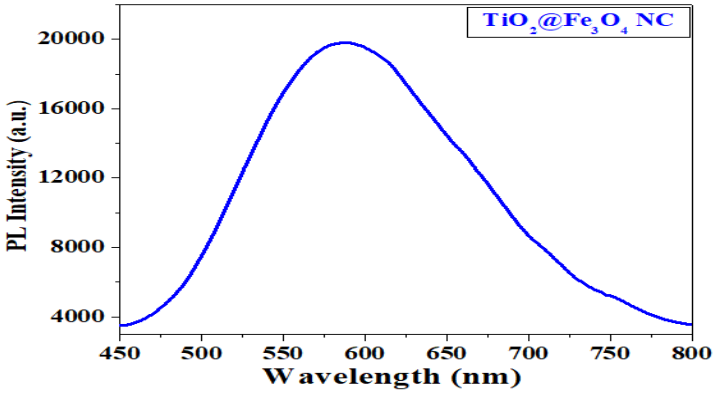


Fig.7: Photoluminescence emission spectrum of the synthesized TiO_2@Fe_3O_4 nanocomposite showing a broad visible emission band centered at about 590 nm.

3.6 Raman Spectroscopy Analysis

The Raman spectrum of the synthesized TiO_2@Fe_3O_4 nanocomposite, recorded over 100–1000 cm^{-1}, is shown in Fig.8. The spectrum exhibits characteristic Raman-active modes of anatase TiO_2 along with Fe_3O_4-related features, confirming the coexistence of both crystalline phases in the nanocomposite (Babudurai et.al., 2018).

The intense Raman band at ~145 cm^{-1} corresponds to the Eg mode of anatase TiO_2, indicating high crystallinity. Additional bands at ~395 cm^{-1} and ~515 cm^{-1} are assigned to the B_{1g} and A_{1g} + B_{1g} vibrational modes of anatase TiO_2, respectively, consistent with its tetragonal crystal structure. The Raman peak positions and their corresponding vibrational mode assignments are summarized in Table 1, further confirming the successful formation and structural integrity of the TiO_2@Fe_3O_4 nanocomposite.

Table 1: Raman peak positions and corresponding vibrational mode assignments for the synthesized TiO_2@Fe_3O_4 nanocomposite.

Raman Shift (cm^{-1})	Vibrational Mode	Phase
~145	E_g	Anatase TiO_2
~395	B_{1g}	Anatase TiO_2
~515	A_{1g} + B_{1g}	Anatase TiO_2
~545–555	T_{2g}	Fe_3O_4 (Magnetite)
~650–670	E_g (TiO_2) + A_{1g} (Fe_3O_4) (overlapping band)	TiO_2 + Fe_3O_4

A weak Raman band at ~540–560 cm^{-1} is assigned to the $T_{2g}(2)$ mode of cubic spinel Fe_3O_4, confirming the magnetite phase. A broader band at ~650–670 cm^{-1} arises from the overlap of the Eg mode of anatase TiO_2 and the A_{1g} mode of Fe_3O_4, reflecting strong interfacial interaction between the two phases. The moderate broadening of the Raman bands is characteristic of nanocrystalline metal oxides and is attributed to the small crystallite size and lattice disorder. No additional peaks associated with secondary phases or impurities were detected, indicating high phase purity. These results are consistent with the XRD analysis and further confirm the successful formation of crystalline TiO_2@Fe_3O_4 nanocomposites suitable for photocatalytic applications (Gnanasekarana et al., 2019).

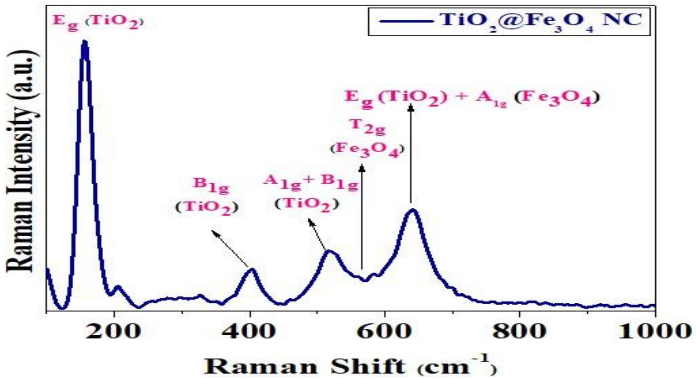


Fig.8: Raman spectrum of the synthesized TiO_2@Fe_3O_4 nanocomposite showing the characteristic vibrational modes of anatase TiO_2 and cubic spinel Fe_3O_4.

3.7 X-ray Photoelectron Spectroscopy (XPS) Analysis

X-ray photoelectron spectroscopy (XPS) was employed to investigate the surface chemical composition and oxidation states of the synthesized TiO_2@Fe_3O_4 nanocomposite. The survey spectrum and high-resolution spectra (Fig.9) show characteristic Ti, Fe, and O peaks with no detectable impurity signals, confirming the high surface purity of the nanocomposite. The binding energies and corresponding chemical-state assignments are summarized in Table 2.

O 1s Spectrum

The O 1s spectrum exhibits a dominant peak at ~528.8 eV, attributed to lattice oxygen (O^{2-}) in Ti–O and Fe–O bonds. A weaker component at 531–532 eV is assigned to surface hydroxyl groups and adsorbed oxygen species. These surface oxygen species provide active sites for pollutant adsorption and facilitate the generation of reactive oxygen species during photocatalysis (Saszet et al., 2025).

Ti 2p Spectrum

The Ti 2p spectrum shows two spin–orbit peaks at ~458.0 eV (Ti $2p_{3/2}$) and ~464.0 eV (Ti $2p_{1/2}$), characteristic of Ti^{4+} in TiO_2. The absence of lower binding-energy peaks indicates negligible Ti^{3+} species, confirming that titanium exists predominantly in the fully oxidized state.

Fe 2p Spectrum

The Fe 2p spectrum displays characteristic peaks at ~710.9 eV (Fe $2p_{3/2}$) and ~724.5 eV (Fe $2p_{1/2}$), along with satellite features typical of mixed Fe^{2+}/Fe^{3+} oxidation states in magnetite (Fe_3O_4). Slight shifts in binding energy are attributed to nanoscale effects and interfacial interactions between the TiO_2 and Fe_3O_4 phases (Thambiliyagodage et al., 2022).

Overall, the XPS results confirm the coexistence of Ti^{4+}, Fe^{2+}/Fe^{3+}, and lattice oxygen, together with surface hydroxyl groups that are beneficial for photocatalytic reactions. These findings agree well with the XRD, FTIR, Raman, and SEM–EDX results, confirming the successful synthesis of high-purity TiO_2@Fe_3O_4 nanocomposites suitable for photocatalytic applications.

Table 2: Binding energies and chemical state assignments of the Ti, Fe, and O core-level XPS spectra of the synthesized TiO_2@Fe_3O_4 nanocomposite.

Spectrum	Binding Energy (eV)	Assignment
Survey	458	Ti 2p
Survey	529	O 1s
Survey	709	Fe $2p_{3/2}$
Survey	722	Fe $2p_{1/2}$
Ti 2p	457.8	Ti $2p_{3/2}$ (Ti^{4+})
Ti 2p	463.3	Ti $2p_{1/2}$ (Ti^{4+})
O 1s	528.8	Lattice oxygen (O^{2-}) in Ti–O and Fe–O bonds
O 1s	531.8	Surface hydroxyl groups (–OH) and adsorbed oxygen species
Fe 2p	708.6	Fe $2p_{3/2}$ (Fe^{2+}/Fe^{3+})
Fe 2p	712.9	Fe $2p_{3/2}$ satellite (shake-up feature)
Fe 2p	722.0	Fe $2p_{1/2}$ (Fe^{2+}/Fe^{3+})
Fe 2p	725.5	Fe $2p_{1/2}$ satellite (shake-up feature)

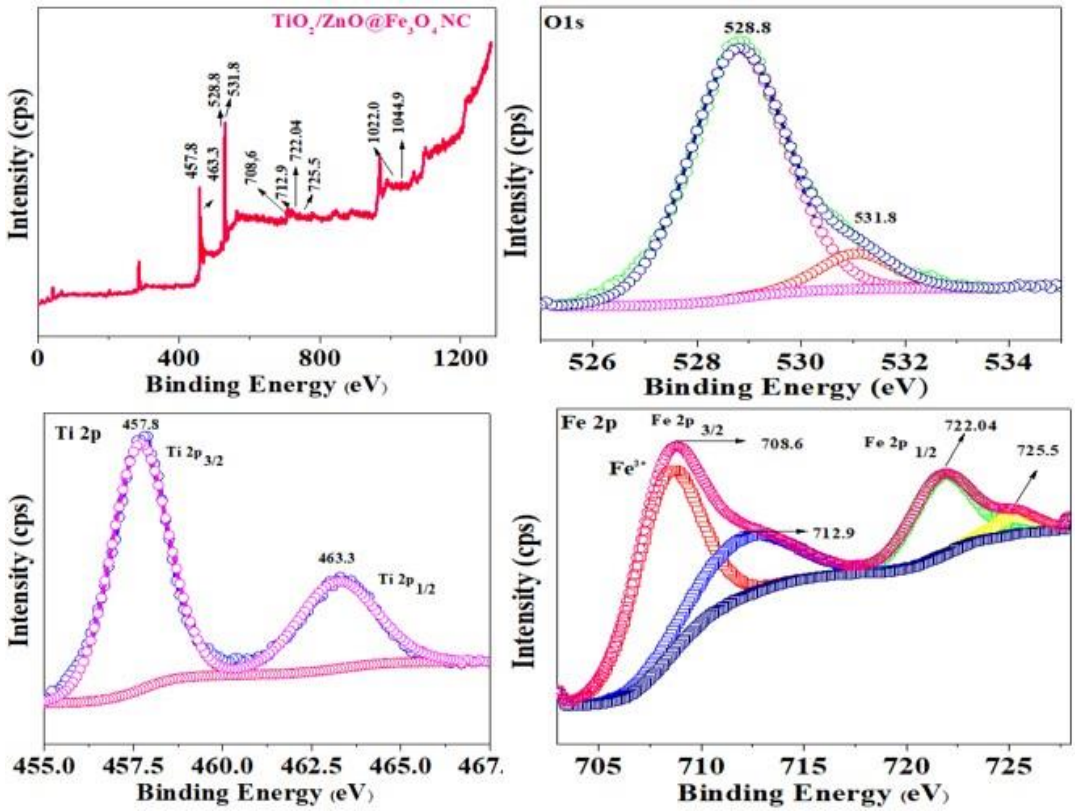


Fig.9: XPS survey and high-resolution spectra of synthesized TiO_2@Fe_3O_4 Nanocomposite showing Ti 2p, Fe 2p, and O 1s core-level spectra.

3.8 Zeta Potential Analysis

The zeta potential of the synthesized TiO_2@Fe_3O_4 nanocomposite was measured to evaluate its surface charge and colloidal stability in aqueous suspension. As shown in Fig.10, the zeta potential distribution exhibits a single, narrow peak centered in the negative region, with a most

probable value of −17.26 mV and a mean zeta potential of −22.15 ± 7.77 mV, indicating a negatively charged surface.

The negative surface charge originates from surface hydroxyl and oxygen-containing functional groups associated with TiO_2 and Fe_3O_4, which provide electrostatic repulsion between particles and contribute to suspension stability. The measured zeta potential indicates moderate colloidal stability, which is typical for metal oxide photocatalysts and sufficient to maintain good dispersion during photocatalytic experiments (Akbiyik et al. 2025). The relatively narrow distribution suggests a uniform surface charge, while the negative surface facilitates the adsorption of cationic dyes such as methylene blue through electrostatic interactions, thereby enhancing photocatalytic degradation.

Overall, the zeta potential results confirm that the synthesized $TiO_2@Fe_3O_4$ nanocomposite possesses a negatively charged, moderately stable surface suitable for aqueous photocatalytic applications, promoting efficient catalyst dispersion and catalyst–pollutant interactions (Yang et al., 2020).

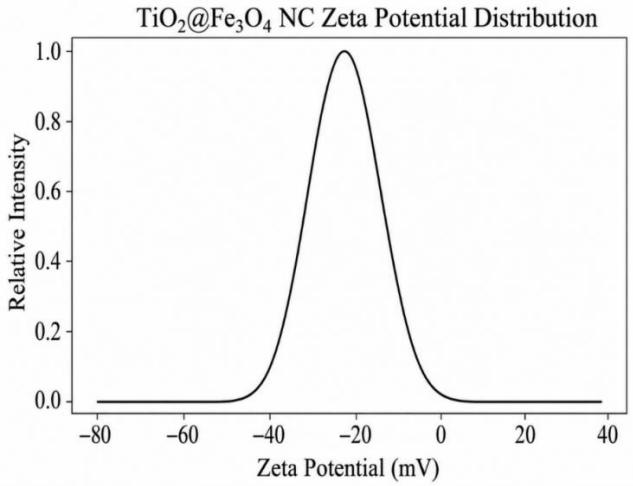


Fig.10: Zeta potential distribution of the synthesized $TiO_2@Fe_3O_4$ nanocomposite showing a negative surface charge and moderate colloidal stability in aqueous suspension.

3.9 Dynamic Light Scattering (DLS) Analysis

The hydrodynamic particle size distribution of the synthesized $TiO_2@Fe_3O_4$ nanocomposite was investigated by Dynamic Light Scattering (DLS), and the corresponding distribution is shown in Fig.11. The DLS profile exhibits a single, narrow intensity peak centered at approximately 1458 nm, indicating a predominant hydrodynamic particle population in aqueous suspension.

The measured hydrodynamic diameter is significantly larger than the crystallite size obtained from XRD because DLS measures the effective particle size in suspension, including the hydration layer and particle aggregates. The relatively large size indicates aggregation of the nanocomposite, which is commonly observed in Fe_3O_4-containing magnetic nanoparticles due to magnetic dipole–dipole and van der Waals interactions, together with adsorption of water molecules on the particle surface (Balasundaram and Annadurai, 2026).

The presence of a single dominant peak suggests a relatively uniform aggregate size distribution. These results are consistent with the zeta potential measurements, which indicated moderate colloidal stability of the suspension.

Overall, the DLS analysis confirms that the $TiO_2@Fe_3O_4$ nanocomposite forms stable hydrodynamic aggregates in aqueous media while retaining nanoscale crystalline domains, as evidenced by XRD and SEM. Such behavior is typical of magnetic nanocomposites and is advantageous for efficient magnetic recovery without significantly affecting photocatalytic performance (Jani and Jain, 2026; Doukeh et al., 2026).

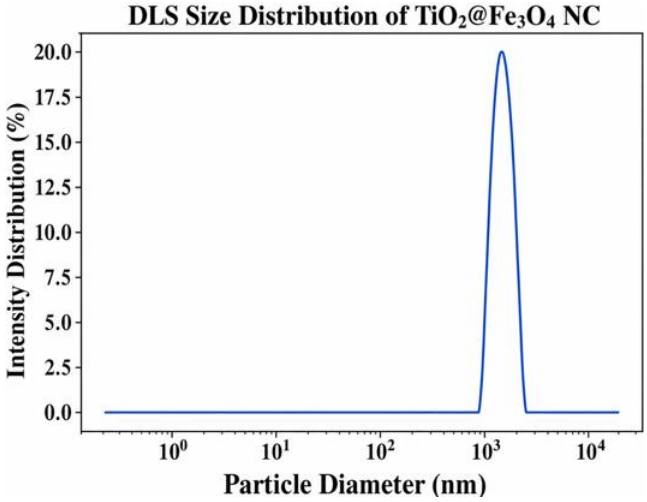


Fig.11: Dynamic Light Scattering (DLS) particle size distribution of the synthesized TiO_2@Fe_3O_4 nanocomposite showing a single dominant hydrodynamic size distribution centered at approximately 1458 nm.

3.10 Photocatalytic Degradation of Organic Dyes Using TiO_2@Fe_3O_4 Nanocomposite

The photocatalytic activity of the synthesized TiO_2@Fe_3O_4 nanocomposite was evaluated using methylene blue (MB), methyl orange (MO), and rhodamine B (RhB) as model organic dyes under UV-C irradiation. Before irradiation, each dye suspension containing the photocatalyst was magnetically stirred in the dark for 1 h to establish adsorption–desorption equilibrium. Photocatalytic degradation was then carried out under continuous UV-C irradiation for 180 min with constant stirring. The degradation process was monitored by UV–Vis spectroscopy at regular intervals. For clarity, only the spectra recorded before dark equilibration, after dark equilibration, and after every 60 min of irradiation are presented in Fig.12. The degradation efficiency was calculated from the change in absorbance at the characteristic maximum absorption wavelength (λ_{max}) of each dye.

3.10.1 Methylene Blue (MB) Degradation

The UV–Vis absorption spectra of methylene blue (MB) in the presence of the TiO_2@Fe_3O_4 nanocomposite are shown in Fig.12(a). MB exhibited a characteristic absorption peak at ≈662 nm, whose intensity decreased progressively with UV irradiation time, indicating continuous photocatalytic degradation. After 180 min, the degradation efficiency reached 67.71%.

The gradual reduction in absorbance without the appearance of new absorption bands suggests successive decomposition of the dye molecules. This photocatalytic activity is attributed to the generation of reactive oxygen species (•OH and $•O_2^-$) under UV irradiation. The TiO_2/Fe_3O_4 heterojunction further enhances charge separation and suppresses electron–hole recombination, thereby improving photocatalytic efficiency (Nengsiha et al., 2024; Fauzi et al., 2024).

3.10.2 Methyl Orange (MO) Degradation

The UV–Vis absorption spectra of methyl orange (MO) during photocatalytic degradation over the TiO_2@Fe_3O_4 nanocomposite are presented in Fig.12(b). MO exhibited a characteristic absorption maximum at approximately 462 nm, corresponding to its azo (–N=N–) chromophore. The absorbance at this wavelength decreased progressively with increasing UV-C irradiation time, indicating continuous degradation of the dye molecules.

After 180 min of irradiation, the TiO_2@Fe_3O_4 nanocomposite achieved a 71.43% degradation efficiency. The gradual decline in absorbance without a significant shift in the absorption maximum suggests the progressive breakdown of the azo chromophore rather than the formation of stable colored intermediates. The degradation is attributed to oxidation by photogenerated reactive oxygen species (•OH and $•O_2^-$) formed on the catalyst surface under UV irradiation. The TiO_2/Fe_3O_4 heterojunction promotes charge separation, suppresses electron–hole recombination, and enhances photocatalytic activity, leading to effective degradation of MO (Sun et al., 2025; Razip et al., 2019).

3.10.3 Rhodamine B (RhB) Degradation

The UV–Vis absorption spectra of RhB in the presence of the TiO_2@Fe_3O_4 nanocomposite are shown in Fig.12(c). The characteristic absorption band at approximately 552 nm decreased progressively with increasing UV-C irradiation time, indicating continuous photocatalytic degradation of the dye.

Among the three investigated dyes, RhB exhibited the highest degradation efficiency (81.40%) after 180 min of irradiation. The superior photocatalytic performance is attributed to the efficient separation of photogenerated charge carriers at the TiO_2/Fe_3O_4 heterojunction, which enhances the generation of reactive oxygen species responsible for dye oxidation. The steady decrease in absorbance confirms the effective decomposition of RhB molecules under UV-C irradiation, demonstrating the excellent photocatalytic activity of the synthesized TiO_2@Fe_3O_4 nanocomposite (Madima et al. 2022).

Overall, the photocatalytic degradation efficiency of the synthesized TiO_2@Fe_3O_4 nanocomposite followed the order:

RhB (81.40%) > MO (71.43%) > MB (67.71%)

The differences in degradation efficiency are attributed to variations in the molecular structure, adsorption affinity, and susceptibility of the dyes to oxidation by photogenerated reactive oxygen species. The progressive decrease in absorbance at the characteristic maximum absorption wavelength (λmax) of each dye confirms the continuous destruction of their chromophoric structures during UV-C irradiation. The degradation efficiency was calculated using:

$$\text{Dye Degradation (\%)} = \left\{\frac{Co - Ct}{Co}\right\} \times 100 \qquad \ldots\ldots (1)$$

where C_0 and C_t are the initial dye concentration and the concentration at irradiation time t, respectively. These results demonstrate that the synthesized TiO_2@Fe_3O_4 nanocomposite is an efficient photocatalyst for degrading both cationic and anionic dyes under UV-C irradiation (Chong et al., 2010).

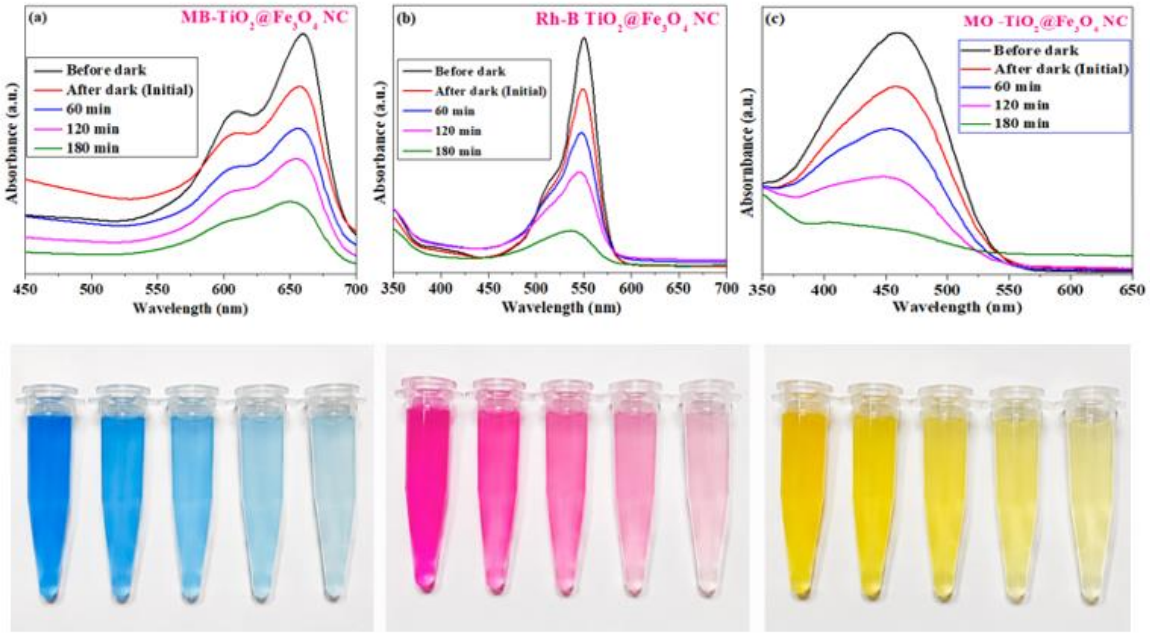


Fig.12: UV–Vis absorption spectra of (a) methylene blue (MB), (b) rhodamine B (RhB), and (c) methyl orange (MO) during photocatalytic degradation over TiO_2@Fe_3O_4 nanocomposites under UV-C irradiation. The photographs below show the corresponding color changes of the dye solutions.

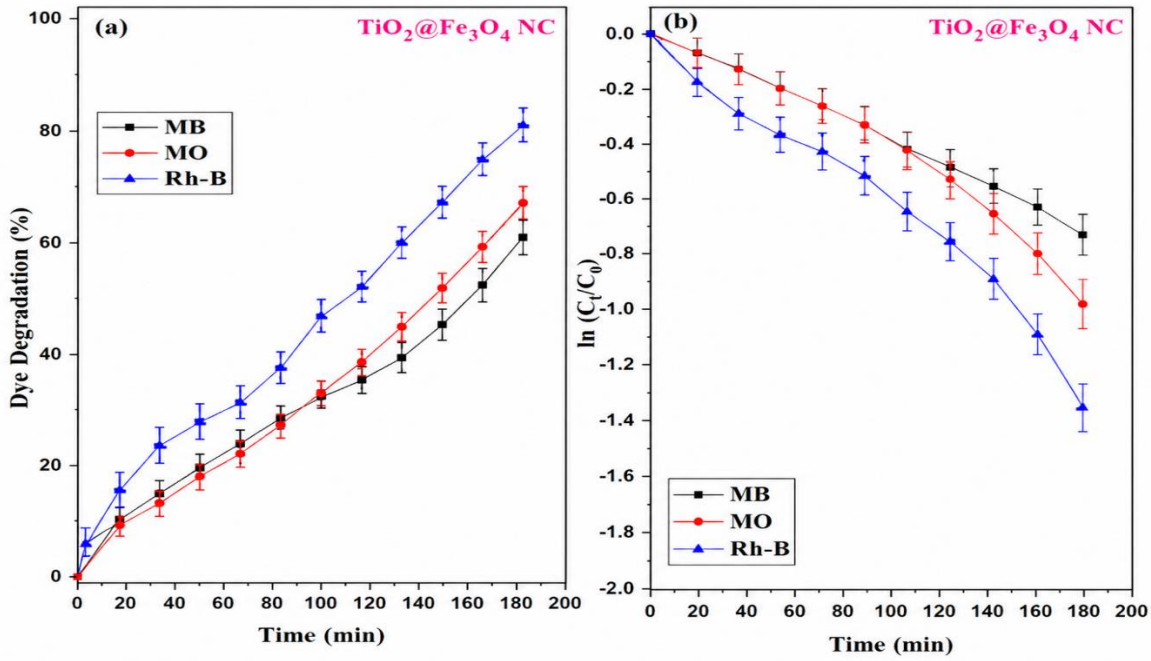


Fig.13. (a) Photocatalytic degradation efficiencies of MB, MO, and RhB over TiO_2@Fe_3O_4 nanocomposites under UV-C irradiation, (b) Corresponding pseudo-first-order kinetic plots.

3.10.4 Photocatalytic Degradation Efficiency and Kinetic Study

The photocatalytic performance of the synthesized TiO_2@Fe_3O_4 nanocomposite was evaluated by degrading MB, MO, and RhB under UV-C irradiation. As shown in Fig.13(a), the degradation efficiency increased steadily with irradiation time for all dyes, owing to the continuous generation of reactive oxygen species (•OH and $•O_2^-$) that oxidize the dye molecules (Hoffmann et al., 1995; Fujishima et al., 2008). After 180 min, degradation efficiencies of 67.71% (MB), 71.43% (MO), and 81.40% (RhB) were achieved, following the order: RhB > MO > MB.

The superior degradation of RhB is attributed to its favorable adsorption behavior and higher susceptibility to oxidation by photogenerated reactive oxygen species (Chong et al., 2010; Chen and Mao, 2007). The enhanced photocatalytic performance of the TiO_2@Fe_3O_4 nanocomposite arises from the TiO_2/Fe_3O_4 heterojunction, which promotes charge separation, suppresses electron–hole recombination, and increases the generation of reactive oxygen species. The magnetic Fe_3O_4 component additionally enables facile recovery and reuse of the photocatalyst, making the nanocomposite attractive for wastewater treatment applications (Herrmann, 1999; Salihi et al., 2022; Saszet et al., 2025; Martínez et al., 2025).

Table 3: Photocatalytic Degradation Performance and Kinetic Parameters of Three Dyes (MB, MO, and RhB).

Dye	Degradation Efficiency (%)	k (min^{-1})	R^2
Methylene Blue (MB	67.71	0.0063	0.984
Methyl Orange (MO)	71.43	0.0070	0.988
Rhodamine B (RhB)	81.40	0.0094	0.995

The degradation kinetics were analyzed using the pseudo-first-order model:

$$\ln(C_0/C_t) = k\,t \qquad \ldots\ldots (2)$$

where C_0 and C_t are the initial and irradiation-time dye concentrations, respectively, and k is the apparent first-order rate constant (Malleshama et al., 2016).

The corresponding kinetic plots (Fig.13(b)) exhibit good linearity, confirming pseudo-first-order degradation kinetics for all dyes. The calculated rate constants were 0.0063 min^{-1} (MB), 0.0070 min^{-1} (MO), and 0.0094 min^{-1} (RhB), with R^2 values of 0.984, 0.988, and 0.995, respectively (Table 3). The highest rate constant for RhB agrees well with its superior degradation efficiency.

Overall, the TiO_2@Fe_3O_4 nanocomposite demonstrates efficient photocatalytic degradation and favorable kinetics, resulting from enhanced charge separation, effective reactive oxygen species generation, and the added advantage of magnetic recoverability, making it a promising photocatalyst for environmental remediation (Chong et al., 2010).

3.10.5 Mechanism of Photocatalytic Degradation of Organic Dyes by TiO_2/Fe_3O_4 Nanocomposites

The photocatalytic degradation of organic dyes by TiO_2/Fe_3O_4 nanocomposites under UV-C irradiation proceeds through the generation of reactive oxygen species (ROS). Upon UV-C irradiation (254 nm), photons with energy greater than the band gap of TiO_2 (~3.2 eV) excite electrons from the valence band (VB) to the conduction band (CB), producing electron–hole pairs:

$$TiO_2 + hv \rightarrow TiO_2\,(e^-CB + h^+VB) \quad \ldots\ldots (3)$$

In the TiO_2/Fe_3O_4 heterojunction, Fe_3O_4 acts as an electron acceptor, promoting charge separation and suppressing electron–hole recombination. The photogenerated electrons reduce dissolved oxygen to form superoxide radicals, while the holes oxidize water molecules or hydroxide ions to generate hydroxyl radicals:

$$e^- + O_2 \rightarrow \bullet O_2^- \quad \ldots\ldots (4)$$

$$h^+ + H_2O \rightarrow \bullet OH + H^+ \quad \ldots\ldots (5)$$

$$h^+ + OH^- \rightarrow \bullet OH \quad \ldots\ldots (6)$$

The superoxide radicals further generate additional reactive species:

$$\bullet O_2^- + H^+ \rightarrow HO_2\bullet \quad \ldots\ldots (7)$$

$$2HO_2\bullet \rightarrow H_2O_2 + O_2 \quad \ldots\ldots (8)$$

$$H_2O_2 + e^- \rightarrow \bullet OH + OH^- \quad \ldots\ldots (9)$$

The highly reactive •OH and $\bullet O_2^-$ radicals oxidize MB, MO, and RhB by breaking their chromophoric structures and aromatic rings, producing intermediate compounds that are ultimately mineralized into harmless products:

$$\text{Organic dye} + \bullet OH/\bullet O_2^- \rightarrow \text{Intermediate products} \rightarrow CO^2 + H^2O + \text{inorganic ions} \quad ..(10)$$

The enhanced photocatalytic activity of the TiO_2/Fe_3O_4 nanocomposite is attributed to the synergistic effect of the heterojunction, which improves charge separation, prolongs charge-carrier lifetime, and increases ROS generation. In addition, the magnetic Fe_3O_4 component enables facile recovery of the photocatalyst using an external magnetic field, enhancing its practical applicability for sustainable wastewater treatment.

The proposed photocatalytic degradation mechanism of organic dyes over the TiO_2/Fe_3O_4 nanocomposite under UV-C irradiation is illustrated in Fig.14.

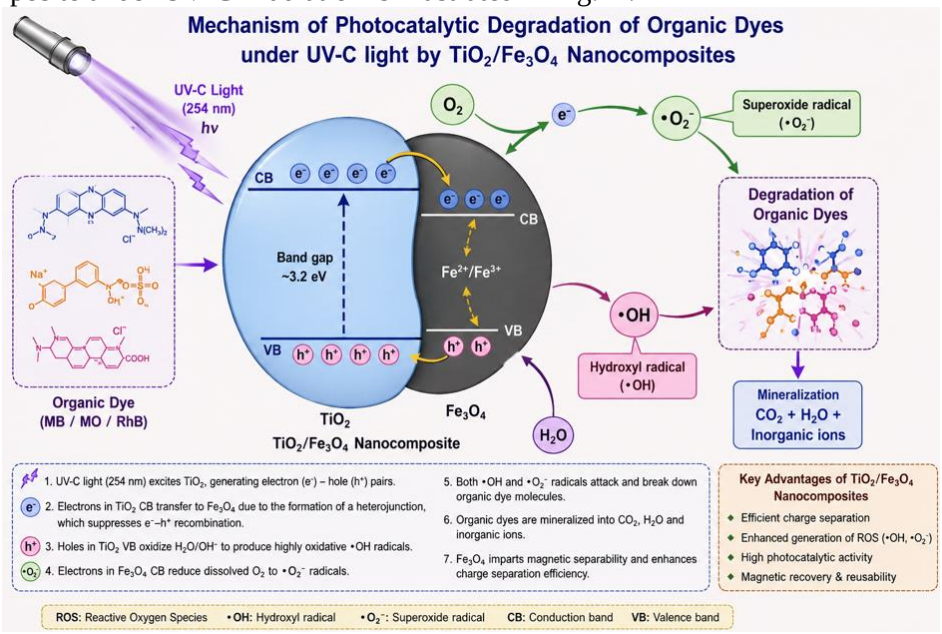


Fig.14: Proposed mechanism of photocatalytic degradation of organic dyes under UV-C irradiation using TiO_2/Fe_3O_4 nanocomposites.

Conclusion

In this study, TiO_2@Fe_3O_4 nanocomposites were successfully synthesized via a simple, cost-effective, and environmentally friendly green route using Trigonella foenum-graecum (fenugreek) leaf extract as a natural reducing and stabilizing agent. Comprehensive characterization confirmed the successful formation of a crystalline TiO_2–Fe_3O_4 heterojunction with desirable structural, optical, thermal, and surface properties.

XRD confirmed the coexistence of anatase TiO_2 and cubic spinel Fe_3O_4 with crystallite sizes of 9.4–17.3 nm. SEM revealed agglomerated porous nanoparticles, while EDX verified the presence of Ti, Fe, and O without detectable impurities. FTIR, Raman, and XPS analyses further confirmed heterojunction formation, good crystallinity, and the presence of Ti^{4+}, Fe^{2+}/Fe^{3+}, oxygen vacancies, and surface hydroxyl groups that favor photocatalytic activity. TGA demonstrated excellent thermal stability, whereas DLS and zeta potential analyses indicated aggregated particles with moderate colloidal stability. PL results suggested efficient charge separation and reduced electron–hole recombination.

The synthesized TiO_2@Fe_3O_4 nanocomposite exhibited excellent photocatalytic performance under UV-C irradiation, achieving degradation efficiencies of 67.71% (MB), 71.43% (MO), and 81.40% (RhB) after 180 min. The degradation followed pseudo-first-order kinetics with rate constants of 0.0063, 0.0070, and 0.0094 min^{-1}, respectively. The enhanced activity is attributed to the TiO_2/Fe_3O_4 heterojunction, which promotes charge separation, suppresses electron–hole recombination, and enhances reactive oxygen species generation. The magnetic Fe_3O_4 component also enables facile catalyst recovery.

Overall, the green-synthesized TiO_2@Fe_3O_4 nanocomposite is a thermally stable, magnetically recoverable, and environmentally sustainable photocatalyst with significant potential for wastewater treatment. Future work should focus on visible-light photocatalysis, catalyst recyclability, mechanistic validation, and performance evaluation in real wastewater systems.

Limitations of the Study

The photocatalytic activity of TiO_2@Fe_3O_4 nanocomposite was evaluated only under UV-C irradiation using model dyes (MB, MO, and RhB). Its performance under visible light, sunlight, and real wastewater conditions was not studied. Catalyst recyclability, long-term stability, degradation intermediates, mineralization, and photocatalytic mechanism require further investigation. Despite these limitations, the nanocomposite demonstrated excellent photocatalytic potential, and future studies should focus on reusability, mechanism validation, and practical wastewater applications.

Acknowledgements

The authors sincerely thank the Director, Materials Group, and Head, Materials Science Division, Bhabha Atomic Research Centre (BARC), Mumbai, India, for providing the research facilities and instrumentation required for this study. The authors acknowledge the support received from Dr. Kartik, Dr. Satish Mishra, Dr. Urmila Maru, Mr. Ajay Chikara, Mr. Shoeb Shaikh, and Mr. Siddharth Gupta of BARC during the experimental work and characterization of the synthesized nanocomposites. The authors also express their sincere gratitude to Ms. Nidhi Pandey and Mr. Samir Momin of BARC for their technical support throughout this work.

Statements & Declarations

Funding:

The authors declare that no external funding was received for this research.

Authors' Contributions:

Author 1 (Azra Ansari): Methodology, Experimental investigation, characterization, data acquisition, formal analysis, and writing—original draft.

Author 2 (Dr. Kulwant Singh): Conceptualization, supervision, methodology, data analysis, interpretation of results, Validation, manuscript review, and editing.

Author 3 (Dr. Nandakishor Chandan): Conceptualization, validation, data analysis.

Author 4 (Dr. Naina Raje): Characterization, data interpretation, validation.

Author 5 (Dr. Celin Achariya): Experimental investigation, validation, data interpretation.

Consent to Publish:
All authors have reviewed the manuscript and consent to its publication.

Ethical Approval:
This is not applicable. This article does not contain any studies involving human participants or animals performed by any of the authors. Therefore, ethical approval was not required.

Consent to Participate:
This is not applicable. This study did not involve human participants.

Competing Interests
The authors declare that they have no known competing financial interests or personal relationships that could have influenced the work reported in this paper.

Data Availability Statement
Not applicable
However, the data supporting the findings of this study are available from the corresponding author upon reasonable request. All relevant data generated or analyzed during this study are included in this published article.

References

1. Acosta I, Zermeño B, Moctezuma E, Rodríguez LFG, Ramírez IJ (2026) Synthesis of Cu–Mo/TiO_2 and Co–Mo/TiO_2 photocatalysts for the efficient degradation of organic pollutants in water. Beilstein J. Nanotechnol. 17:559-570 https://doi.org/10.3762/bjnano.17.37
2. Aguinaco A, Mánuel JM, Blanco E, Domínguez M, Litrán R, Delgado JJ, Solar MRD (2022) Fe_3O_4-TiO2 Thin films in solar photocatalytic processes. Materials 15(19):6718. https://doi.org/10.3390/ma15196718
3. Ahmed S, Ahmad M, Swami BL, Ikram S (2016) A review on plants extract mediated synthesis of silver nanoparticles for antimicrobial applications: A green expertise. J. Adv. Res. 7(1):17-28. https://doi.org/10.1016/j.jare.2015.02.007
4. Akbiyik H, Girgin A, Zaman1 BT, Atako A, San N, Bakirdere S (2025) The usage of TiO_2@Fe_3O_4 nanocomposites synthesized by a novel and facile method as adsorbents in the separation/ preconcentration of silver ions from domestic wastewater samples. J. Adv. Res. 16:23. https://doi.org/10.1186/s40543-025-00495-z
5. Almutairi ST (2024) Fabrication and catalytic activity of TiO_2/Fe_3O_4 and Fe β-cyclodextrin nanocatalysts for safe treatment of industrial wastewater. Heliyon 10:e35400. https://doi.org/10.1016/j.heliyon.2024.e35400
6. Babudurai M, Maya RH, Solís M, Thomas CT, Velumani S (2018) Photocatalytic degradation of Orange G using TiO_2/Fe_3O_4 nanocomposites, J. Mater. Sci.: Mater. Electron. 29(8):15436–15444. https://doi.org/10.1007/s10854-10854-018-9069-1
7. Balasundaram A, Annadurai T (2026) Biofabrication, characterization and efficacy of copper oxide nanoparticles derived from Caesalpinia bonducella Linn. in combating breast cancer. Next Nanotechnol. 9:100539. https://doi.org/10.1016/j.nxnano.2026.100539
8. Banisharif A (2013) TiO_2/Fe_3O_4 Nanocomposite photocatalysts for enhanced photo-decolorization of congo red dye. Int. J. Nanosci. Nanotechnol. 9(4):193-202. https://doi.org/10.13140/2.1.4217.5369
9. Chen X, Mao SS (2007) Synthesis Titanium dioxide nanomaterials: properties, modifications and applications. Chem. Rev. 107(7):2891-2959. https://doi.org/10.101/cr0500535
10. Chong MN, Jin B, Chow CWK, Saint C (2010) Recent developments in photocatalytic water treatment technology: A review. Water Res. 44(10):2997-3027. https://doi.org/10.1016/j.watres.2010.02.039
11. Deng Y, Zhao R (2015) Advanced oxidation process (aops) in waste water treatment. Curr. Pollut. Rep. 1(3):167-176. https://doi.org/10.1007/s40726-015-0015-z
12. Denga RM, Lucey MM, Baloyi J, Mbaya R (2025) Synthesis and characterization of Fe_3O_4@TiO_2@Zeolite nanocomposite adsorbent for the removal of Levoflaxin antibiotic

from environmental water matrices. J. Iran. Chem. Soc. 22(1):113-128. https://doi.org/10.1007/s13738-024-03135-2

13. Doukeh R, Eparu CN, Prundurel AP, Tudose M, Brănoiu G, Ghețiu IV, Păun LS, Mihai S, Stan IG, Stoica DB (2026) Synthesis, characterization, and performance evaluation of nanocrystalline metal oxides for shale inhibition in water-based drilling fluids. Sustain. Chem. 7(1):3. https://doi.org/10.3390/suschem7010003
14. Fauzi RA, Istiqomah NI, Sari EK, Suharyadi E, Aliah H (2024) Concentration dependences of photocatalytic activity in green-synthesis Fe_3O_4/TiO_2 nanocomposite utilizing moringa oleifera for methylene blue dye degradation. J. Phys.: Conf. Ser. 2696(1):012011. https://doi.org/10.1088/1742-6596/2696/1/012011
15. Fujishima A, Tryk X, Zhang DA (2008) TiO_2 photocatalysis and related surface phenomena. Surf. Sci. Rep. 63(12):515-582. https://doi.org/10.1016/j.surfrep.2008.10.001
16. Gebrezgiabher M, Gebreslassie G, Gebretsadik T, Yeabyo G, Elemo F, Bayeh Y, Thomas M, Linert W (2019) A C-doped TiO_2/Fe_3O_4 nanocomposite for photocatalytic dye degradation under natural sunlight irradiation. J. Compos. Sci. 3(3):75. https://doi.org/10.3390/jcs3030075
17. Gnanasekarana L, Hemamalini R, Rajendran S, Qinc J, Yolad ML, Atare N, Gracia F (2019) Nanosized Fe_3O_4 incorporated on a TiO_2 surface for the enhanced photocatalytic degradation of organic pollutants. J. Mol. Liq. 287:110967. https://doi.org/10.1016/j.molliq.2019.110967
18. Goldstein JI, Newbury DE, Michael JR., Ritchie NWM, Scott JHJ., Joy DC (2018) Scanning electron microscopy and x-ray microanalysis. Microsc. Microanal. 4(1):550. https://doi.org/10.1017/S1431927618015271
19. Hashimoto K, Irie H, Fujishim A (2005) TiO_2 Photocatalysis: a historical overview and future prospects. Jpn. J. Appl. Phys. 44(12R):8269. https://doi.org/10.1143/JJAP.44.8269
20. Henderson MA (2011) A surface science perspective on TiO_2 photocatalysis. Surf. Sci. Rep. 66(6-7):185-297. https://doi.org/10.1016/j.surfrep.2011.01.001
21. Herrmann JM (1999) Heterogeneous photocatalysis: fundamentals and applications to the removal of various types of aqueous pollutants. Catal. Today, 53(1):115-129. https://doi.org/10.1016/S0920-5861(99)00107-8
22. Hoffmann MR, Martin ST, Choi W, Bahnemann DW (1995) Environmental applications of semiconductor photocatalysis. Chem. Rev. 95(1):69-96. https://doi.org/10.1021/cr00033a004
23. Iravani S (2011) Green synthesis of metal nanoparticles using plants. Green Chem. 13(10):2638-2650. https://doi.org/10.1039/c1gc15386b
24. Jani M, Jain P, hydrothermal (2026) A comparative assessment of the quality of TiO_2 nanoparticles synthesized through green, sol–gel and solvothermal techniques using Citrus limon. Next Mater. 12:102384. https://doi.org/10.1016/j.nxmate.2026.102384
25. Khashan SA, Dagher S, Tit N, Alazzam A, Obaidat I (2017) Novel method for synthesis of Fe_3O_4@TiO_2 core/shell nanoparticles. Surf. Coat. Technol. 322:92-98. https://doi.org/10.1016/j.surfcoat.2017.05.045
26. Kubiak A (2023) Comparative study of TiO_2–Fe_3O_4 photocatalysts synthesized by conventional and microwave methods for metronidazole removal. Sci. Rep. 13(1):12075. https://doi.org/10.1038/s41598-023-39342-9
27. Kubiak A, Kubacka M, Gabała E, Dobrowolska A, Synoradzki K, Ciesielczyk KS, Czaczyk K, Jesionowski T (2020) Hydrothermally assisted fabrication of TiO_2-Fe_3O_4 composite materials and their antibacterial activity. Materials 13(21):4715. https://doi.org/10.3390/ma13214715
28. Laurent S, Forge D, Port M, Roch A, Robic C, Elst LV, Muller RN (2008) Magnetic iron oxide nanoparticles: synthesis, stabilization, vectorization, physicochemical characterizations, and biological applications. Chem. Rev. 108(6):2064-2110. https://doi.org/10.1021/cr068445e
29. Madima N, Kefeni KK, Mishra SB, Kuvarega AT (2022) Fabrication of magnetic recoverable Fe_3O_4/TiO_2 heterostructure for photocatalytic degradation of rhodamine B dye. Inorg. Chem. Commun. 145:109966. https://doi.org/10.1016/j.inoche.2022.109966

30. Malleshama B, Sudarsanamb P, Reddy BVS, Reddy BM (2016) Development of cerium promoted copper–magnesium catalysts for biomass valorization: Selective hydrogenolysis of bioglycerol. Appl. Catal. B Environ. 181:47-57. https://doi.org/10.1016/j.apcatb.2015.07.037
31. Martínez IÁ, Cardoso-Avila PE, Zarazúa I, Guevara PLD, Pérez-Tavares JA, González-Aguiñaga E, Patakfalvi R (2025) Photocatalytic evaluation of Fe_2O_3–TiO_2 nanocomposites: influence of TiO_2 content on their structure and activity. Molecules 5, 30(21):4309. https://doi.org/10.3390/molecules30214309
32. Mehdinia A, Shoormeij Z, Jabbari A (2017) Trace determination of lead (II) ions by using a magnetic nanocomposite of the type Fe_3O_4/TiO_2/PPy as a sorbent, and FAAS for quantitation. Microchim. Acta 184(5):1529-1537. https://doi.org/10.1007/s00604-017-2156-9
33. Moosavi S, Li RYM, Lai CW, Yusof Y, Gan S, Akbarzadeh O, Chowhury ZZ, Yue XG, Johan MRB (2020) Degradation methylene blue dye photocatalytic degradation over synthesised Fe_3O_4/AC/TiO_2 nano-catalyst: degradation and reusability studies. Nanomaterials 10(12):2360. https://doi.org/10.3390/catal12090986
34. Nengsiha S, Abdulmadjid SN, Mursal M, Jalilc Z (2024) Photocatalytic performance of Fe_3O_4-TiO_2 in the degradation of methylene blue dye: Optimizing the usability of natural iron sand. Mater. Sci. Energy Technol. 7:374-380. https://doi.org/10.1016/j.mset.2024.06.001
35. Oladipo AA, Mustafa FS (2023) Bismuth-based nanostructured photocatalysts for the remediation of antibiotics and organic dyes. Beilstein J. Nanotechnol. 14(1):291-321. https://doi.org/10.3762/bjnano.14.26
36. Pucar G, Nikić J, Gvoić V, Mandic AK, Agbaba J, Tomin MB, Kerkez DV (2022) Photocatalytic degradation of magenta effluent using magnetite doped TiO_2 in solar parabolic trough concentrator. Catalysts 12(9):986. https://doi.org/10.3390/catal12090986
37. Ramadhan M, Pradipta AR, Kunarti ES (2017) Synthesis of Fe_3O_4/TiO_2-Co nanocomposite as model of photocatalyst with magnetic properties. Mater. Sci. Forum 901:14-19
38. Razip NIM, Lee KM, Lai CW, Ong BH (2019) Recoverability of Fe_3O_4/TiO_2 nanocatalyst in methyl orange degradation. Mater. Res. Express 6(7):075517. https://doi.org/10.4028/www.scientific.net/MSF.901.14
39. Salihi SA, Bayati M, Jasim AM, Fidalgo M, Xing Y (2022) Magnetic mesoporous TiO_2/Fe_3O_4 nanocomposite adsorbent for removal of sulfamethazine from water. Environ. Adv. 9:100283. https://doi.org/10.1016/j.envadv.2022.100283
40. Saszet K, Guliman S, Szalma L, Székely I, Tetean R, Todea M, Szamosvölgyi Á, Pop MM, Tudoran LB, Magyari K, Pop LC, Pap Z, Baia L (2025) Recyclable TiO_2–Fe_3O_4 magnetic composites for the photocatalytic degradation of paracetamol: comparative effect of pure anatase and mixed-phase P25 TiO_2. Catalysts 15(9):839. https://doi.org/10.3390/catal15090839
41. Sembiring T, Lubis H, Simanjuntak R, Lubis RY, Sebayang K, Marlianto E, Saragih MK Hasanah M (2025) Synthesis and characterization of magnetic Fe3O4/TEOS/TiO2 composites for methylene blue photodegradation. Adv. J. Chem. Sect. 8:930-947. https://doi.org/10.48309/AJCA.2025.464679.1576
42. Sun L, Li Z, Yuan Z, Liu Y, Liu Y, Mei S, Meng F, Ouyang X, Xiong Y, Zhang K, Chen Z (2025) Fe_3O_4@SiO_2@Fe-TiO_2 Preparation of magnetic photocatalyst, solution photocatalytic degradation performance of methyl orange in Na_2SO_4. Appl. Sci. 15(7):3781. https://doi.org/10.3390/app15073781
43. Thambiliyagodage C, Usgodaarachchi L, Jayanetti M, Liyanaarachchi C, Kandanapitiye M, Vigneswaran S (2022) Efficient visible-light photocatalysis and antibacterial activity of TiO_2-Fe_3C-Fe-Fe_3O_4/graphitic carbon composites fabricated by catalytic graphitization of sucrose using natural ilmenite. ACS Omega 7(29):25403. https://doi.org/10.1021/acsomega.2c02336
44. Vinosel VM, Janifer MA, Anand S, Pauline S (2017) Structural and functional group characterization of nanocomposite Fe_3O_4/TiO_2 and its magnetic property. Mech. Mater. Sci. Eng. 9(1). https://hal.science/hal-01499407v1

45. Wojciechowska A, M.Szczupak A, Szczupak AM, Bieluń ZL (2022) TiO_2-modified magnetic nanoparticles (Fe_3O_4) with antibacterial properties. Materials 15(5):1863. https://doi.org/10.3390/ma15051863
46. Yang Z, Wu W, Yu L, Fan X, Yu Y (2020) Fabrication and characterization of magnetically responsive Fe_3O_4@TiO_2 core-shell adsorbent for enhanced thallium removal. Environ. Sci. Pollut. Res. 27(24):30518-30529. https://doi.org/10.1007/s11356-020-09144-x